Continuous far-field zone focusing of flexural waves through phase engineering of metagratings

Zhanrui Tan and Jun Mei*
Department of Applied Physics, School of Physics, South China University of Technology, Guangzhou 510640, China

(Received 5 February 2026; accepted 20 July 2026; published 3 August 2026)

Continuous far-field zone focusing of flexural wave is highly desirable for applications such as structural health monitoring, energy harvesting, and advanced sensing. In this work, we propose a metalens design paradigm capable of focusing flexural wave across a continuous zone in the far-field region. The metalens is based on an intelligently designed metagrating, in which each unit cell consists of two elliptical holes etched through a thin aluminum plate. Each unit is designed to deflect the incoming waves along a prescribed direction with tunable reflection phase and near-unitary reflection efficiency. The metagrating is engineered such that different unit cells direct the incident wave toward distinct subregions within the target focusing zone. When the reflection phase is uniformly maintained across the metagrating, a continuous extended focusing zone is formed through the superposition of wave beams reflected from all unit cells. This approach achieves a focusing area of approximately $2900\lambda^2$ in the far field, with an average intensity enhancement factor of 9.0 and an almost homogeneous intensity distribution. The compact planar architecture of the metalens not only offers a flexible and practical solution for far-field zone focusing, but also holds promise as a versatile planar component suitable for system integration.

DOI: 10.1103/k8wt-lybx

I. INTRODUCTION

The precise manipulation and efficient focusing of elastic waves in solid plates are of critical importance in numerous fields, including nondestructive testing, structural health monitoring, advanced sensing, and energy harvesting. Most existing studies have been centered on "point-focusing" functionality, in which incident wave energy is concentrated around a single focal point [1–15]. With the development of metamaterials, focusing capabilities have recently been extended to "needle-focusing" and "curved-path-focusing" scenarios. In these configurations, wave energy is deliberately concentrated along a straight line or a predesigned curved trajectory, typically through the use of specially engineered wave fronts such as Airy beams and self-accelerating Bessel beams [16,17]. Nevertheless, focusing incident wave energy within a continuous two-dimensional zone—i.e., concentrating energy over an extended area rather than around a discrete point or along a one-dimensional curve—remains an open challenge. In application contexts such as nondestructive testing and energy harvesting, the capability to focus wave energy over a designed continuous two-

*Contact author: phjunmei@scut.edu.cn

Published by the American Physical Society under the terms of the Creative Commons Attribution 4.0 International license. Further distribution of this work must maintain attribution to the author(s) and the published article's title, journal citation, and DOI.

dimensional region presents inherent advantages, including enhanced efficiency in defect scanning and improved rates of energy conversion, thereby highlighting the practical significance of this functionality.

Conventionally, wave-front manipulation has relied primarily on phase accumulation along the propagation path, achieved through refractive or diffractive components to realize focusing functions. However, such structures are typically bulky and costly to fabricate, therefore failing to meet the demands for portability and cost-effectiveness. In this context, metasurfaces offer a distinct and promising alternative for wave-front control [18–32]. By tailoring the local phase response of subwavelength-thick unit cells, nearly arbitrary control over transmitted or reflected wave fronts can, in principle, be achieved. Nevertheless, passive gradient metasurfaces face fundamental limitations. Based on the generalized Snell's law (GSL), they often exhibit a sharp decline in scattering efficiency at large steering angles due to significant impedance mismatch [33]. Moreover, focusing functionality typically requires that all wave fronts arriving at the focal spot be precisely in phase to ensure constructive interference. While this approach is feasible for point-focusing and curve-focusing applications, it is considerably more difficult to implement in zone-focusing scenarios, where simultaneous and continuous phase manipulation across a two-dimensional region remains highly challenging, if not impractical.

To overcome these limitations, a concept of metagratings has recently emerged in the literature [34–37]. This distinct design paradigm is grounded in grating diffraction theory rather than the GSL. Its fundamental principle involves the intelligent design of individual unit cells to efficiently and exclusively channel incident wave energy into a limited set of designated diffraction orders. Unlike gradient metasurfaces, which typically require discrete subwavelength structures to approximate a continuous phase or impedance profile, metagratings eliminate this approximation step. Notably, metagratings can sustain nearly unitary deflection efficiency in wave-front manipulation, even for steep diffraction angles. This capability is particularly beneficial for achieving high-efficiency zone focusing over large areas. Consequently, this approach not only significantly improves wave-front control performance but also streamlines both design and fabrication processes. Furthermore, it opens avenues for achieving diverse and advanced functionalities, such as anomalous reflection [38–45], anomalous refraction [46–50], asymmetrical or nonreciprocal transmission [51–55], multifunctional devices [56,57], cloaking [58–60], omnidirectional retroreflection [61,62], acoustic vortices [63,64], and beam focusing [65–72].

In this work, we propose a metagrating-based metalens design paradigm for the continuous zone focusing of flexural waves in the far field. The metagrating comprises a planar array of unit cells, each featuring two elliptical holes etched through a thin aluminum plate. By synergistically applying diffraction grating theory and multiobjective optimization algorithms, each unit cell is meticulously designed to channel the incident wave energy exclusively into a predetermined diffraction order. Crucially, and to the best of our knowledge, for the first time in a metagrating, we demonstrate simultaneous, independent control over both the reflection amplitude and reflection phase at the individual unit cell level. By enforcing a constant reflection phase profile across the entire aperture, we successfully realize a continuous, efficient, and uniform two-dimensional zone-focusing functionality. As a proof of concept, the designed metalens achieves a focused area of approximately $2900\lambda^2$ in the far field with an average intensity enhancement factor of 9.0. This represents a significant departure from traditional point- or curve-focusing schemes, advancing the field toward applications that demand large-area, high-efficiency wave-energy regulation. Furthermore, the compact, planar architecture of the metalens not only provides a practical and flexible solution for far-field wave manipulation, but also positions it as a versatile, integrable component for advanced acoustic or elastic wave systems.

II. THEORETICAL ANALYSIS AND RESULTS

To achieve the zone-focusing function of flexural wave, high energy density must be distributed and confined within a specified continuous region of the thin plate, rather than forming a discrete

point or linear focus. The aim is to generate an extended and uniform focal zone with substantially enhanced field intensity, which is advantageous for applications including energy harvesting and structural health monitoring. Without loss of generality, we consider a thin aluminum plate with a thickness of 1 mm, having Young's modulus $E = 70$ GPa, Poisson's ratio $\nu = 0.33$, and mass density $\rho = 2700$ kg/m^3. The operating frequency is 6 kHz, corresponding to a flexural wavelength of $\lambda = 40.38$ mm.

We begin with grating diffraction theory. When a plane wave impinges on a grating, it is reflected or refracted along several discrete diffraction channels. For a flexural wave incident at an angle θ_{in}, the directions of reflected wave channels satisfy

$$k \times \sin\theta_{\text{in}} + m\frac{2\pi}{d} = k \times \sin\theta_{\text{re}}, \tag{1}$$

where $k = 2\pi/\lambda$ is the wave number of the flexural wave, $m = 0, \pm 1, \pm 2, \ldots$ represents the diffraction order, d is the grating period, and θ_{re} denotes the reflection angle.

When $d < 2\lambda$ and for the case of normal incidence ($\theta_{\text{in}} = 0^\circ$), the diffraction order m can only take the values 0 and ± 1. Equation (1) then reduces to

$$d \times \sin\theta_{\text{re}} = m\lambda \ (m = 0, \pm 1). \tag{2}$$

Using Eq. (2), we can design all unit cells in the right half of the metagrating, because the left half is simply a mirror of the right half. Each unit cell in the right half is designed to reflect the incident wave exclusively into the $m = -1$ diffraction channel.

To achieve a zone-focusing effect, different unit cells should redirect the incident wave along different directions, i.e., toward different subregions within the focusing zone. In this way, a continuous and extended focusing zone can be formed by the superposition of all wave beams reflected by the individual unit cells. To realize this, we assign L focal points to L unit cells, meaning each unit cell corresponds to a single focal point. Specifically, the $m = -1$ reflected wave from the Lth unit cell is directed to converge at the Lth focal point, with a focal length given by $F_L = F_1 + (L-1)\Delta F$, as illustrated in Fig. 1. Here, ΔF represents the distance between adjacent focal points, and θ_L denotes the reflection angle of the Lth unit cell.

We begin with the first unit cell. To ensure that $|m| = 1$ is the highest diffraction order, we set $\theta_1^{(m=-1)} = -31^\circ$ (if $|\theta_1^{(m=-1)}| < 30^\circ$, higher orders such as $|m| = 2$ will appear in the reflected wave, making the design of metagrating more challenging). To simplify the notation, we use θ_L to represent $\theta_L^{(m=-1)}$ in this work.

According to Eq. (2), $d_1 = 78.40$ mm. We set r, the distance from lens axis to the first unit cell, as 50λ. In this way, $F_1 = \frac{r+\frac{d_1}{2}}{\tan(|\theta_1|)} = 84.83\lambda$, enabling us to achieve a far-field zone-focusing effect.

To balance the size of the focusing zone and the energy concentration factor, we set $\Delta F = 0.5\lambda$. Therefore, the focal length of the second unit cell is $F_2 = F_1 + \Delta F$. The distance of the second unit cell to the lens axis is $r + d_1$. Thus, we have $F_2 = \frac{r+d_1+\frac{d_2}{2}}{\tan(|\theta_2|)}$. It follows that the reflection angle θ_2 is determined by $\theta_2 = -\tan^{-1}\frac{r+d_1+\frac{d_2}{2}}{F_2} = 31.79^\circ$, and the period d_2 can be obtained using Eq. (2).

Applying the above analysis to the Lth unit cell, we have

$$\tan(|\theta_L|) = \frac{r + \sum_{i=1}^{L-1} d_i + \frac{d_L}{2}}{F_1 + (L-1)\Delta F}. \tag{3}$$

Combining Eq. (3) with Eq. (2), we can uniquely determine the diffraction angle θ_L and period d_L for the Lth unit cell.

To realize high-efficiency focusing, each unit cell is designed with two elliptical holes etched through the thin plate, as shown in Fig. 1. Each ellipse is defined by five geometric parameters: the semimajor axis a_i, semiminor axis b_i, angle φ_i between a_i and x axis, and its center coordinates (x_i, y_i), where $i = 1, 2$. Thus, we have ten adjustable parameters for each unit cell. Using an intelligent optimization algorithm, these parameters can be optimized to exclusively direct the

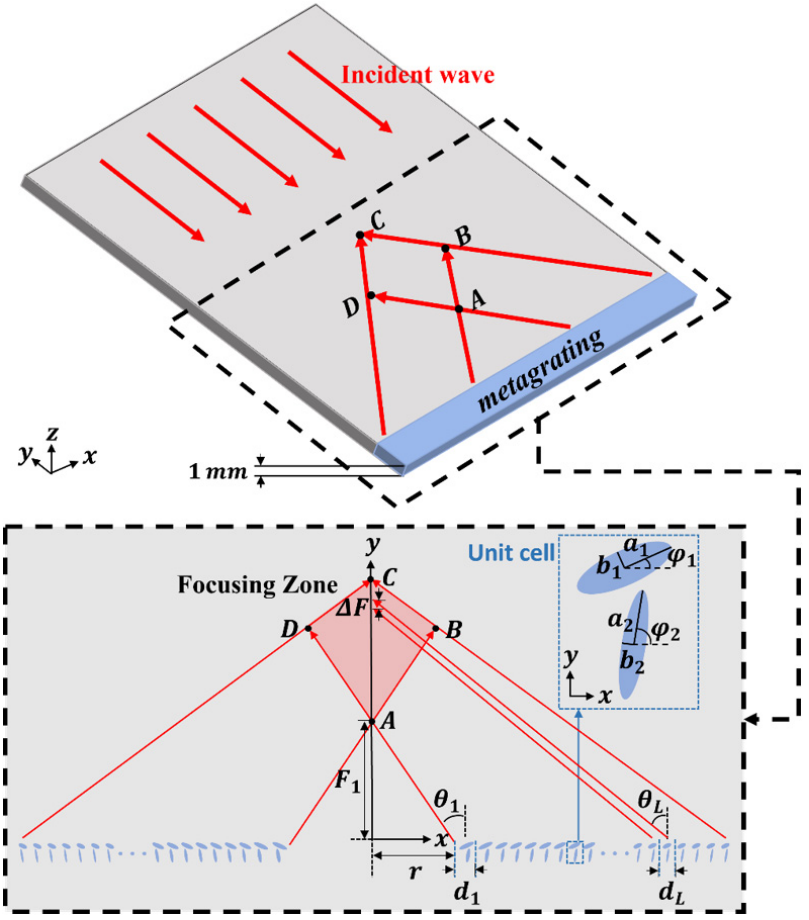


FIG. 1. Schematic of a metagrating lens. Each unit cell contains two elliptical holes drilled through the thin plate. The Lth unit is designed to reflect a normally incident plane wave with at an angle θ_L toward to the Lth focal point. Different unit cells reflect the incident wave along different directions, as indicated by red arrows. The distance between adjacent focal points is ΔF. All reflected waves combine to form an extended focal zone (shaded in red) with a high wave-energy factor, bounded by the edges AB, BC, CD, and DA connecting the four vertices A, B, C, and D.

incident wave into the $m = -1$ diffraction channel. A key advantage of this metagrating is that the diffraction efficiency can approach 100% even at large deflection angles—a critical requirement for high-efficiency focusing in large numerical aperture (NA) metalenses, yet difficult to achieve with conventional gradient metasurfaces.

As a first example, we construct a metagrating lens consisting of 300 unit cells in total. The design can be significantly simplified by leveraging mirror symmetry with respect to the lens axis: Only the parameters of the 150 unit cells on the right half need to be specified, while the left half can be obtained by mirror reflection. Using a genetical algorithm (GA), the geometrical parameters for these 150 unit cells are optimized and explicitly listed in Table I.

To further simplify the optimization and design process, we divide the 150 unit cells into 16 groups, with each group sharing the same set of geometrical parameters (e.g., a_i, b_i, and φ_i). This grouping is justified because when the diffraction angle θ_L is sufficiently large, the difference between θ_L and θ_{L+1} becomes very small. Consequently, by slightly adjusting the grating period

TABLE I. The geometric parameters for each unit cell in the metagrating shown in Fig. 3.

No.	L	Θ_L(deg)	a_1(mm)	b_1(mm)	x_1(mm)	y_1(mm)	φ_1(deg)	a_2(mm)	b_2(mm)	x_2(mm)	y_2(mm)	φ_2(deg)
1	1	31.00	32	8	1	130	76	34	8	−4	180	16
2	2	31.79	46	6	10	137	64	33	14	−1	180	18
3	3, 4	32.54–33.25	35	5	8	117	76	36	7	0	179	18
4	5, 6	33.93–34.58	32	7	9	129	77	36	5	0	178	14
5	7, 8	35.19–35.78	31	9	6	131	80	34	11	1	176	20
6	9–11	36.35–37.41	45	14	−1	105	78	31	6	−1	187	19
7	12–16	37.91–39.72	35	18	7	133	81	31	7	−2	178	21
8	17–23	40.14–42.36	31	6	7	132	87	31	7	1	172	21
9	24–32	42.69–45.02	29	7	3	116	75	28	9	−2	178	22
10	33–41	45.27–47.12	25	9	−9	134	95	26	5	−3	187	21
11	42–50	47.33–48.82	28	6	−8	111	79	26	7	3	180	23
12	51–67	49.00–51.31	40	15	−8	120	91	26	10	−1	190	25
13	68–84	51.44–53.16	27	10	−5	130	65	19	6	−7	186	23
14	85–100	53.26–54.52	23	7	−2	133	87	25	7	1	178	26
15	101–135	54.59–56.67	30	7	−1	126	72	26	7	0	181	28
16	136–150	56.72–57.36	28	6	−9	125	93	26	5	0	178	25

from d_L to d_{L+1}, the set of parameters of the Lth unit cell can also satisfy the designated function of the $(L+1)$th unit cell, namely, directing the incident wave toward the specified focal point. This approach significantly simplifies the optimization and design of the metagrating.

Two representative unit cells (specifically, the 1st and 20th) are illustrated in Fig. 2(a), under normally incident planar flexural wave from above. The scattered field distributions of the out-of-plane displacement w exhibit well-preserved planar wave fronts that are precisely directed along the designated angles $\theta_1 = 31^\circ$ and $\theta_{20} = 41.30^\circ$, respectively. In Fig. 2(b), the reflection efficiency R_L (i.e., $R_L^{(m=-1)}$) along the $m = -1$ diffraction channel is plotted against the unit cell index L, demonstrating nearly unitary reflection efficiency across the design.

We then assembled a metagrating-based metalens comprising 300 unit cells (150 per half), with a projected focusing area of approximately $2900\lambda^2$. Full wave numerical simulations were performed using COMSOL Multiphysics. An out-of-plane (i.e., z direction) force load was applied as the source to excite the incident flexural wave. Figure 3(a) plots the normalized displacement intensity

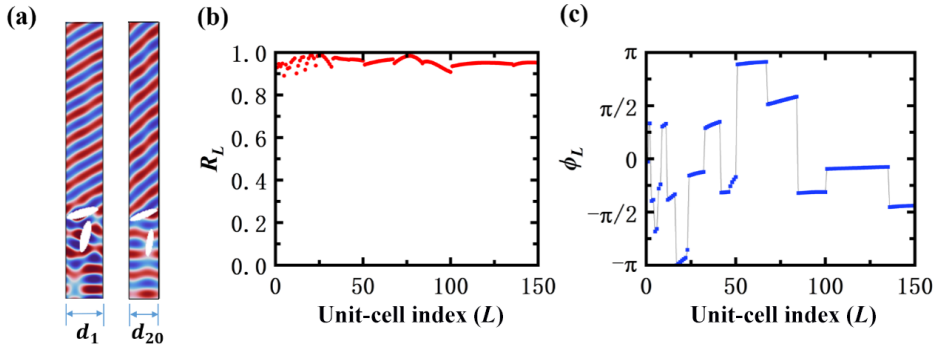


FIG. 2. Design of the metagrating unit cell. (a) Schematic diagram of two representative unit cells and their scattered field distributions. (b) The reflection efficiency R_L along the $m = -1$ diffraction channel as a function of the unit cell index L. (c) The reflection phase ϕ_L as a function of the unit cell index L, assuming incident wave phase $\phi_0 = 0$.

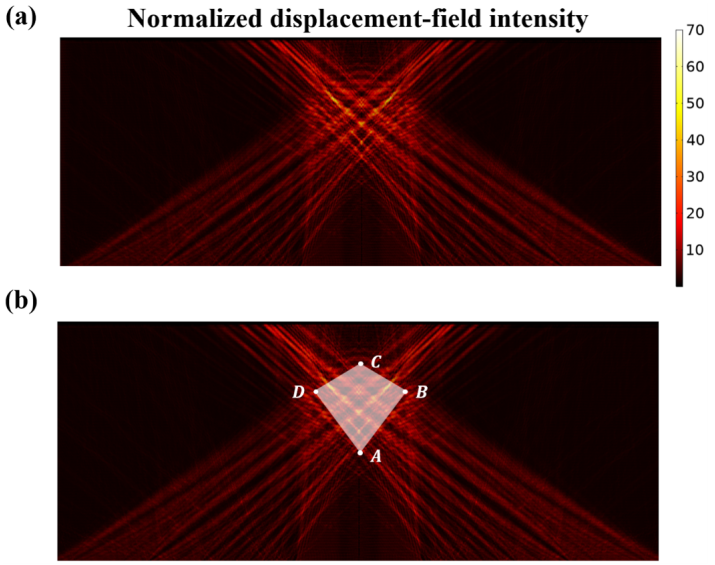


FIG. 3. The focusing effect of the metalens. (a) Normalized displacement field intensity $|w|^2/|w_0|^2$ for a normally incident wave beam. Panel (b) is the same as panel (a) except that a white region is highlighted, which corresponds to the projected focal region ABCD in Fig. 1.

$|w|^2/|w_0|^2$, where w represents the resulting out-of-plane displacement field in the presence of metalens and w_0 denotes the displacement field of the incident wave. The figure shows that although the reflected wave beam from each unit cell follows the intended direction, the superposition of all the beams does not produce a relatively uniform and homogeneous focal region as anticipated. Instead, clear intensity fluctuations are observed within the focusing zone. Calculations show that the average normalized intensity of the displacement field inside the white region of Fig. 3(b)—the expected focusing area surrounded by the first and last unit cells of the left and right halves—is given by $\frac{1}{S}\int(|w|^2/|w_0|^2)dxdy = 7.4$, where S is the area of white region.

We attribute this inhomogeneity in wave intensity to the interference among wave fronts reflected by different unit cells. Specifically, the incident plane wave can be expressed as $A_0[\exp(i\vec{k}_0 \cdot \vec{r})]$, where A_0 and $\vec{k}_0$ represent the amplitude and wave vector of incident wave, respectively, and $|\vec{k}_0| = \frac{2\pi}{\lambda}$ is the wavenumber. Under normal incidence, $\vec{k}_0$ is oriented along the negative y direction. The wave beam reflected by the Lth unit cell can be written as $A_L[\exp(i(\vec{k}_L \cdot \vec{r} + \phi_L))]$, where A_L and $\vec{k}_L$ represent the amplitude and wave vector of the reflected wave, respectively, and ϕ_L denotes the phase of the reflected wave relative to the incident wave, assuming the incident wave phase $\phi_0 = 0$.

In the initial metalens design, the wavevector $\vec{k}_L$ was aligned with the $m = -1$ diffraction order to achieve near-unity reflection efficiency ($A_L \approx A_0$), while the reflection phase ϕ_L was not actively controlled. As shown in Fig. 2(c), the reflection phase ϕ_L exhibits considerable variation across different unit cells. We hypothesize that the observed suboptimal focusing performance arises from these variations in the relative reflection phase between unit cells, and that such phase inhomogeneity is the primary cause of the pronounced intensity fluctuations in the focal region. To overcome this limitation, we propose an improved design strategy that allows independent and simultaneous control of both the amplitude A_L and the phase ϕ_L at each unit cell, while maintaining the condition that $\vec{k}_L$ couples exclusively into the $m = -1$ diffraction channel.

Based on this rationale, we define the reflection efficiency R_L and reflection phase ϕ_L along the $m = -1$ diffraction channel as the optimization objectives. The target is to simultaneously achieve near-unity R_L and a constant ϕ_L across all unit cells. Specifically, we aligned the reflection phase ϕ_L

TABLE II. The geometric parameters for each unit cell in the metagrating shown in Fig. 5.

No.	L	Θ_L(deg)	a_1(mm)	b_1(mm)	x_1(mm)	y_1(mm)	φ_1(deg)	a_2(mm)	b_2(mm)	x_2(mm)	y_2(mm)	φ_2(deg)
1	1	31.00	33	9	2	131	76	34	8	−4	180	16
2	2	31.79	30	8	8	136	82	34	13	−1	175	17
3	3, 4	32.54–33.25	36	7	12	116	85	35	8	−1	181	17
4	5, 6	33.93–34.58	35	8	6	133	81	34	11	−2	178	18
5	7, 8	35.19–35.78	31	8	4	135	78	34	12	1	178	17
6	9–11	36.35–37.41	32	5	5	135	81	32	7	0	182	19
7	12–16	37.91–39.72	32	7	2	128	83	33	6	0	183	20
8	17–23	40.14–42.36	27	6	11	126	81	29	6	−1	182	21
9	24–32	42.69–45.02	29	7	3	116	75	28	9	−2	178	22
10	33–41	45.27–47.12	27	7	−6	128	77	28	5	−1	183	23
11	42–50	47.33–48.82	24	8	−7	107	106	26	9	2	179	26
12	51–67	49.00–51.31	25	9	4	144	71	27	4	0	184	25
13	68–84	51.44–53.16	25	5	0	141	71	24	8	−3	178	26
14	85–100	53.26–54.52	24	6	−2	132	89	24	6	−1	181	23
15	101–150	54.59–57.36	30	7	−1	126	72	26	7	0	181	28

from the 2nd to the 150th unit cell with the reflection phase ϕ_1 of the 1st unit cell and defined $\Delta\phi_L = |\phi_L - \phi_1|$. A multiobjective GA was employed to minimize $\Delta\phi_L$ while simultaneously driving R_L toward 100%. The resulting optimized parameters are explicitly listed in Table II.

The detailed hyperparameters for the multiobjective GA are set as follows: population size = 400, max generations = 150, crossover fraction = 0.8, migration fraction = 0.2, migration interval = 20, Pareto fraction = 0.35, and constraint tolerance = 1e-6. During the optimization process, the multiobjective GA evaluates and ranks the fitness of individuals within each generation of the population. After multiple evolutions, it ultimately finds a set containing multiple noninferior solutions, known as the Pareto front, from which the global optimization parameters can be selected.

To address the trade-off between efficiency and phase deviation, we adopt a two-step approach. In the first step, the geometrical parameters of each unit cell are optimized to maximize the reflection efficiency along the $m = -1$ channel, denoted as R_L. A threshold is set such that $R_L > 0.9$. Consequently, as many unit cell configurations as possible satisfying this high-efficiency criterion are retained. In the second step, from the library of configurations obtained in the first step, we impose a narrow allowable variation range on the reflection phase, i.e., $|\phi_L - \phi_1| \leqslant 0.1\pi$. Through this two-step procedure, both high reflection efficiency and a nearly uniform reflection phase are achieved across the metalens.

Figure 4 shows the optimized reflection efficiency R_L and reflection phase ϕ_L for each unit cell, demonstrating excellent performance across the metalens.

Using the newly designed unit cells, we assembled the metalens and evaluated its performance. The resulting normalized displacement intensity $|w|^2/|w_0|^2$ is plotted in Fig. 5, where a clear intensity enhancement is observed within the focal region. Compared with the initial design, the optimized metalens exhibits significantly improved uniformity in the intensity distribution within the focal zone. We calculated the spatially averaged normalized intensity over the target focusing zone [white region in Fig. 3(b)] as $\frac{1}{S}\int(|w|^2/|w_0|^2)dxdy$, obtaining a value of 9.0, which is notably higher than that of the initial design.

The above results indicate that a homogeneous reflection phase contributes to a uniform wave intensity distribution within the focal region. To further validate the hypothesis that intensity nonuniformity originates from reflection phase variations across unit cells, we conduct a control experiment. Specifically, we designed two metalenses with deliberately introduced abrupt transitions in the reflection phase ϕ_L—one with a single transition [Fig. 6(a)] and another with two transitions

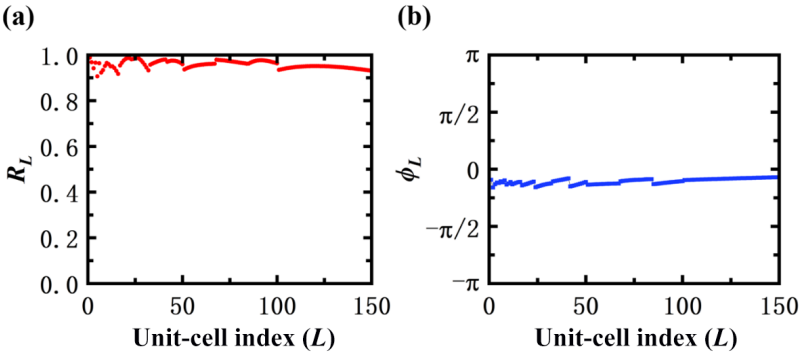


FIG. 4. Further optimization of the metagrating unit cells. (a) The reflection efficiency R_L along the $m = -1$ diffraction channel as a function of the unit cell index L. (b) The reflection phase ϕ_L as a function of the unit cell index L.

[Fig. 6(b)]. The corresponding normalized displacement intensities $|w|^2/|w_0|^2$ distributions are shown in Figs. 7(a) and 7(b), respectively.

Compared with the optimized metalens (Fig. 5), both control designs exhibit distinct features. First, noticeable discontinuities (dark regions between bright wave beams) appear in the wave propagation paths from the unit cells to the focal region. Second, the intensity distribution within the focal region becomes visibly less uniform. Third, the spatially averaged normalized intensity values are calculated to be 8.8 and 8.7, respectively, both lower than the value of 9.0 achieved by the optimized design. Fourth, a larger number of phase discontinuities correlates with degraded focusing performance, in terms of both intensity homogeneity and enhancement within the focal region.

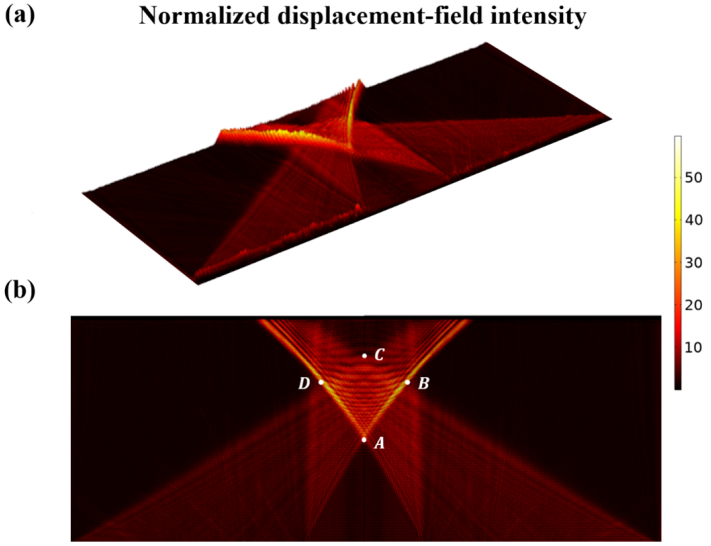


FIG. 5. Normalized displacement field intensity $|w|^2/|w_0|^2$ for the phase-homogenized metalens, where its 3D view and 2D view are shown in panels (a) and (b), respectively. In panel (b) A, B, C, and D mark the four vertices of the continuous focusing zone.

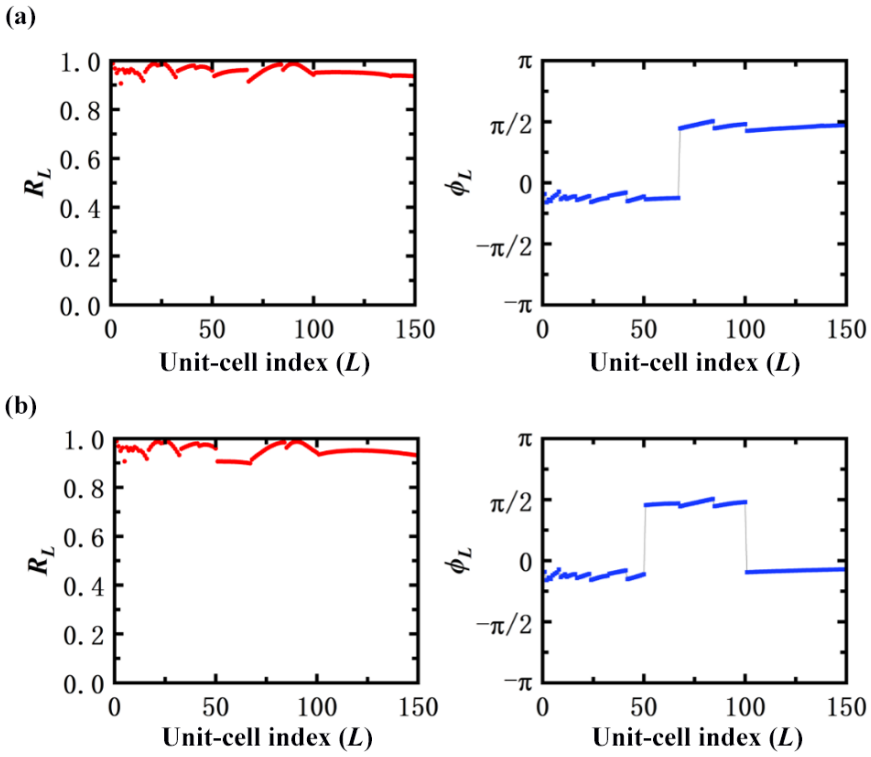


FIG. 6. Another two designs of the metalens with different phase modulations. (a) The reflection efficiency R_L and reflection phase ϕ_L for the first new design, where one abrupt change is intentionally introduced in ϕ_L. Panel (b) shows the second new design where two abrupt changes are intentionally introduced in ϕ_L.

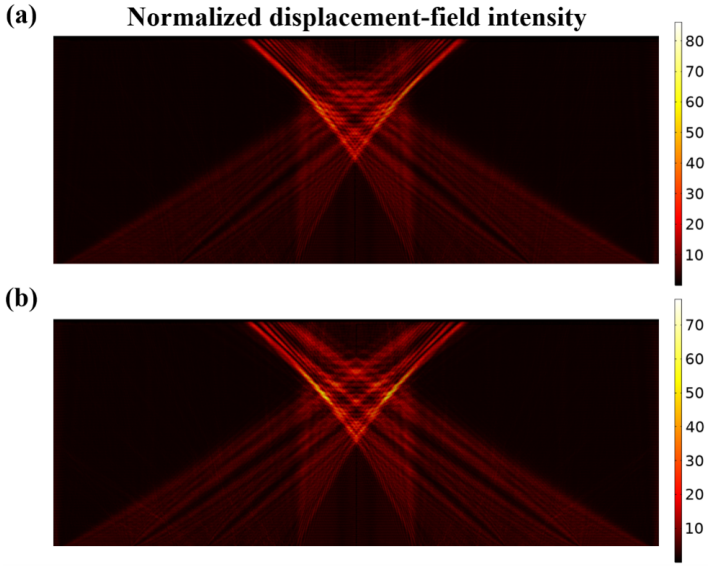


FIG. 7. The effect of ϕ_L modulation. Panels (a) and (b) show the normalized displacement field intensity $|w|^2/|w_0|^2$ corresponding to Figs. 6(a) and 6(b), respectively.

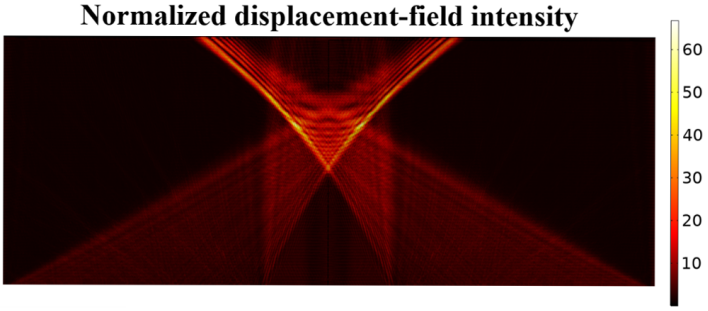


FIG. 8. Normalized displacement field intensity $|w|^2/|w_0|^2$ for a new metalens design, where a smaller focusing area and a higher field intensity enhancement factor are obtained.

Overall, this control experiment confirms that variation in reflection phase ϕ_L adversely affects focusing quality, underscoring the critical role of phase uniformity in achieving a high-performance metalens with a large focusing area, strong intensity enhancement, and improved intensity uniformity.

In the previous paragraphs, the operation frequency is set to 6 kHz as an example to illustrate the design paradigm and the focusing effect. It should be noted, however, that the operating frequency can be shifted to higher values. A discussion on the scalability of the metalens is given in Appendix A.

Moreover, the design of the metalens involves a trade-off between the focusing area and the intensity enhancement. As illustrated in Fig. 8, the distance (ΔF) between adjacent focal points is deliberately reduced from 0.5λ to 0.4λ compared to the configuration in Fig. 5, leading to a smaller reflection angle (θ_L) for each unit cell. Consequently, a smaller focusing area of approximately $1900\lambda^2$ is achieved. Correspondingly, the average normalized displacement field intensity within the focal region increases to 10.3, compared to 9.0 in the previous case. This trend can be understood from energy conservation: Because the NA of the metalens is unchanged, the total wave energy incident on the metagrating remains the same. A reduction in the focal area, resulting from the adjustment of ΔF, therefore leads to a higher energy enhancement factor. Thus, by appropriately tuning ΔF, the focusing area and enhancement level can be flexibly tailored for different application requirements. To this end, a quantitative discussion on the trade-off between focal area and intensity enhancement is given in Appendix B.

We note that in current research on metagratings, nearly all studies focus on high-efficiency manipulation of the reflection efficiency R_L along a specific diffraction channel to realize attractive functionalities. To the best of our knowledge, little attention has been paid to the corresponding reflection phase ϕ_L. This work demonstrates that controlling phase ϕ_L is equally important as controlling R_L. As a vivid example, we illustrate the achievement of a zone-focusing function. We believe that the simultaneous control of R_L and ϕ_L opens possibilities for realizing of more advanced and novel wave manipulation functionalities.

Furthermore, we have performed a robustness analysis of the metalens system with respect to frequency and disorder; the details are provided in Appendix C.

III. CONCLUSIONS AND DISCUSSIONS

To conclude, we propose a metagrating-based metalens capable of achieving continuous zone focusing of flexural waves in the far field. The metalens is formed by a metagrating consisting of an array of unit cells, each featuring two elliptical holes etched into a thin aluminum plate. Leveraging grating diffraction theory and multiobjective optimization, each unit cell is independently designed to redirect normally incident plane waves into specified diffraction orders, such that both the

TABLE III. Focusing area versus normalized displacement field intensity.

ΔF	0.5λ	0.45λ	0.4λ	0.3λ
Focusing area (λ^2)	2900	2400	1900	1100
Average normalized displacement field intensity	9.0	9.4	10.3	12.3

reflection phase and reflection efficiency can be concurrently controlled. These unit cells collectively concentrate wave energy into different subzones within the target focal region. By deliberately maintaining a uniform reflection phase across the entire metagrating, the superposition of the reflected wave beams forms a continuous zone-focusing profile in the far field, characterized by high efficiency and minimal intensity fluctuation. Notably, both the focusing area and the average wave-intensity enhancement factor can be tailored by engineering the reflection direction of each unit cell, providing a flexible platform for meeting specific application needs.

Owing to its planar and straightforward architecture, combined with unprecedented far-field zone-focusing capabilities, the proposed metalens holds promise for applications in structural health monitoring, energy harvesting and transfer, and advanced sensing. Here, we highlight the unique advantages that point focusing cannot provide, as illustrated by two practical industrial scenarios.

In structural health monitoring and nondestructive testing, large-area focusing acts as a wide inspection "brush" rather than a slow scanning "needle." It enables single-shot detection of defects (e.g., cracks and delamination) over a broad region, such as a several-centimeter strip on aircraft wings or wind turbine blades. In contrast, conventional point focusing requires time-consuming scanning and risks missing defects located between scan points. Large-area focusing dramatically increases inspection speed, eliminates blind spots, and improves detection reliability.

Furthermore, large-area focusing distributes energy uniformly over an extended region, such as several square centimeters. This allows moving or rotating components—including engine blades, gear systems, or sensors inside sealed containers—to receive power without requiring micron-level alignment precision, while avoiding local thermal damage caused by the extreme energy density associated with point focusing. Robust operation under vibration or rotation is inherently guaranteed.

These unique capabilities make large-area focusing particularly valuable in scenarios where point focusing is inefficient, alignment critical, or potentially destructive.

DATA AVAILABILITY

The data that support the findings of this article are not publicly available upon publication because it is not technically feasible and/or the cost of preparing, depositing, and hosting the data would be prohibitive within the terms of this research project. The data are available from the authors upon reasonable request.

APPENDIX A: SCALABILITY OF THE METALENS

In the previous discussions, the operation frequency is set to 6 kHz as an example to illustrate the design paradigm and the focusing effect. It should be noted, however, that the operating frequency can be shifted to higher values. When the frequency increases from 6 kHz to a substantially higher value, e.g., 0.6 MHz, the zone-focusing functionality can still be achieved due to the scalability

TABLE IV. Focusing performance of the metalens as a function of frequency.

Frequency (kHz)	5.7	5.8	5.9	6.0	6.1	6.2	6.3
Focusing area (λ^2)	2000	2400	2500	2900	2900	3100	3600
Average normalized displacement field intensity	7.6	8.3	8.9	9.0	8.3	7.4	6.3

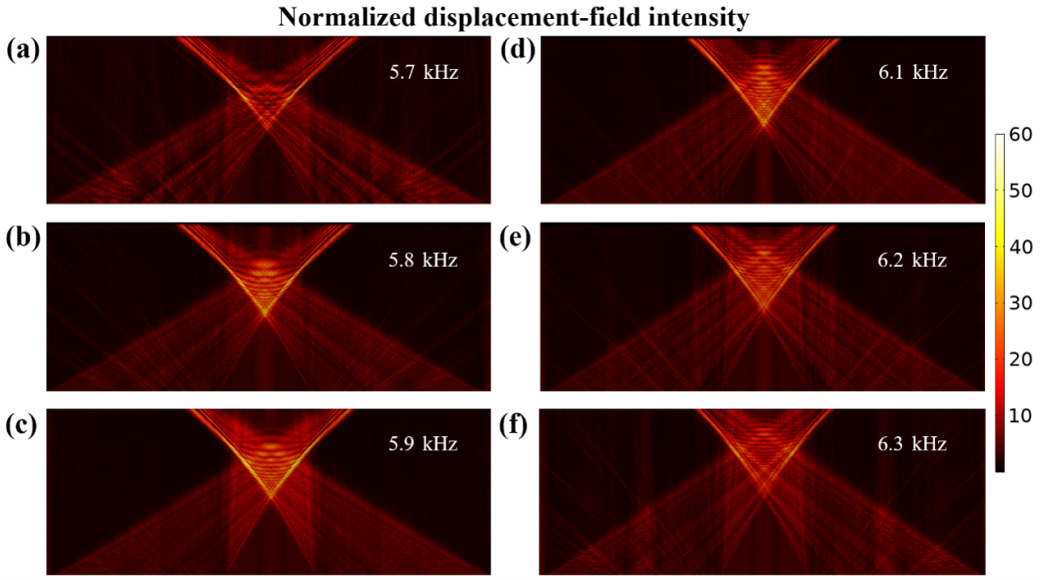


FIG. 9. The focusing effect of the metalens at frequencies of 5.7, 5.8, 5.9, 6.1, 6.2, and 6.3 kHz.

of the metagrating design. A key feature is that there is no universal constant constraining the dimensions of the metagrating; the dynamic wave equation is scale invariant. Consequently, design configurations at different frequencies differ only by a uniform contraction or expansion of all distances. Specifically, at the original operating frequency $f_1 = 6$ kHz, the flexural wavelength is λ_1. If we increase the frequency to $f_2 = 0.6$ MHz, the corresponding wavelength becomes λ_2. To achieve similarly high-efficiency focusing performance, we need only multiply all original length parameters of the unit cell (e.g., $a_1,\ b_1, a_2,\ b_2$) by the scaling factor $\frac{\lambda_2}{\lambda_1}(\approx 0.08)$. While a 1 mm precision suffices for the design at λ_1, a precision of 0.01 mm is adequate for the scaled design at λ_2. Fortunately, such dimensional accuracy is achievable with current fabrication technologies, as demonstrated in the literature [45].

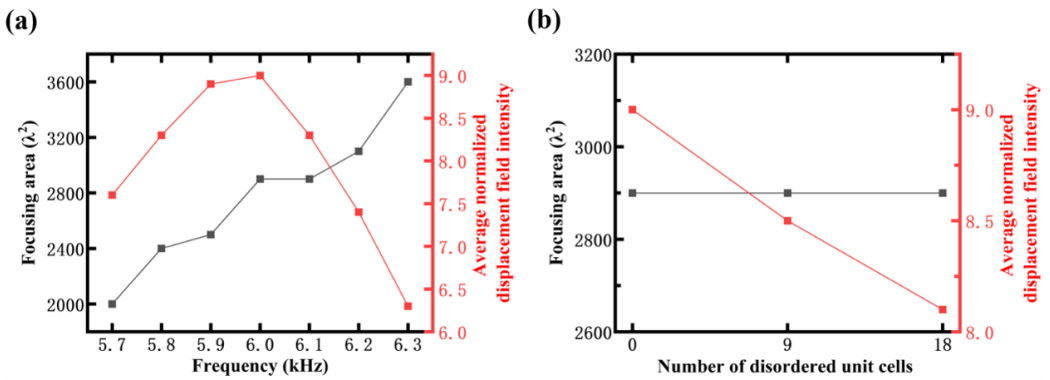


FIG. 10. Focusing performance of the metalens as a function of (a) frequency and (b) the disorder parameter.

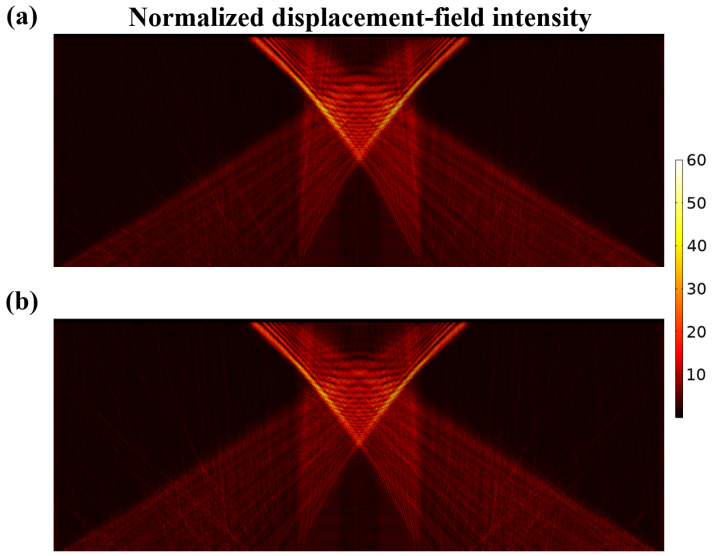


FIG. 11. Normalized displacement field intensity $|w|^2/|w_0|^2$ of a disordered metalens. In panels (a) and (b), 9 and 18 unit cells, respectively, are deliberately modified using the parameters $a_1 = 30$ mm, $b_1 = 6$ mm, $x_1 = 0$ mm, $y_1 = 120$ mm, $\varphi_1 = 90^\circ$, $a_2 = 22$ mm, $b_2 = 6$ mm, $x_2 = 0$ mm, $y_2 = 180$ mm, and $\varphi_2 = 0^\circ$. Notably, robust far-field focusing persists despite the introduced disorder.

APPENDIX B: TRADE-OFF BETWEEN FOCAL AREA AND INTENSITY ENHANCEMENT

In the main part of the paper, we present two metalens designs with $\Delta F = 0.5\lambda$ (Fig. 3) and $\Delta F = 0.4\lambda$ (Fig. 8), respectively, leading to focusing areas of $2900\lambda^2$ and $1900\lambda^2$. Their average normalized displacement field intensities are 9.0 and 10.3, respectively. For quantitative analysis, two additional metalens designs are introduced with $\Delta F = 0.45\lambda$ and $\Delta F = 0.3\lambda$, corresponding to focusing areas of $2400\lambda^2$ and $1100\lambda^2$, respectively. All four designs are listed in Table III.

By fitting the data, the relationship between the average normalized displacement field intensity (denoted as I) and the focusing area (denote as $A\times\lambda^2$) can be expressed as $I = C_2A^2 + C_1A + C_0$ with $C_2 = 7.10\times10^{-7}$, $C_1 = -4.68\times10^{-3}$, and $C_0 = 16.6$. the quadratic term is negligible ($|C_2| \ll |C_1|$), making the relationship nearly linear.

APPENDIX C: ROBUSTNESS ANALYSIS

We have performed a robustness analysis of the metalens system with respect to frequency and disorder. Although the metalens was initially designed for an operating frequency of 6.0 kHz, it is found to perform well at neighboring frequencies. Figure 9 illustrates the focusing performance of the metalens at 5.7, 5.8, 5.9, 6.1, 6.2, and 6.3 kHz, demonstrating that a frequency-robust far-field zone-focusing effect is achieved.

Using the field patterns in Fig. 9, we quantitatively characterize the frequency-dependent focusing performance of the metalens, with key metrics compiled in Table IV. For a fair comparison,

TABLE V. Focusing performance of as a function of the disorder parameter.

Number of disordered unit cells	0	9	18
Focusing area (λ^2)	2900	2900	2900
Average normalized displacement field intensity	9.0	8.5	8.1

the focusing area is normalized by λ^2, where λ denotes the wavelength of the flexural wave at the design frequency of 6 kHz. As indicated in Table IV, the normalized focusing area increases monotonically with frequency. In contrast, the average normalized displacement field intensity reaches its maximum at 6 kHz, which corresponds to the designed operating frequency, and gradually decreases as the frequency deviates from this value. These data are represented by the red and black dots in Fig. 10(a), respectively.

To investigate the influence of disorder, we deliberately modified the geometrical parameters of selected unit cells within the metalens. Figure 11 presents the resulting flexural wave patterns for two disorder configurations: 9 unit cells (indices 1, 10, 25, 48, 60, 94, 115, 116, and 139) in panel (a) and 18 unit cells (indices 1, 3, 10, 25, 26, 33, 37, 48, 60, 70, 72, 88, 94, 115, 116, 122, 139, and 147) in panel (b). Each modified unit cell was assigned the following parameters: $a_1 = 30$ mm, $b_1 = 6$ mm, $x_1 = 0$ mm, $y_1 = 120$ mm, $\varphi_1 = 90^\circ$, $a_2 = 22$ mm, $b_2 = 6$ mm, $x_2 = 0$ mm, $y_2 = 180$ mm, and $\varphi_2 = 0^\circ$.

As shown in Fig. 11, robust far-field zone-focusing persists in both cases, confirming the metalens's resilience against geometric disorder. Quantitatively, Table V indicates that the average normalized displacement field intensity decreases monotonically with increasing disorder count—a trend also reflected by the red and black data points in Fig. 10(b).

[1] J. Zhao, B. Bonello, and O. Boyko, Focusing of the lowest-order antisymmetric lamb mode behind a gradient-index acoustic metalens with local resonators, Phys. Rev. B **93**, 174306 (2016).

[2] M. Zheng, C. Il, X. Liu, R. Zhu, G. Hu, and Y. Y. Kim, Non-resonant metasurface for broadband elastic wave mode splitting, Appl. Phys. Lett. **116**, 171903 (2020).

[3] L. Cao, Z. Yang, Y. Xu, Z. Chen, Y. Zhu, S.-W. Fan, K. Donda, B. Vincent, and B. Assouar, Pillared elastic metasurface with constructive interference for flexural wave manipulation, Mech. Syst. Signal Process. **146**, 107035 (2021).

[4] W. Wang, J. Iglesias, Y. Jin, B. Djafari-Rouhani, and A. Khelif, Experimental realization of a pillared metasurface for flexural wave focusing, APL Mater. **9**, 051125 (2021).

[5] Y. Jin, W. Wang, A. Khelif, and B. Djafari-Rouhani, Elastic metasurfaces for deep and robust subwavelength focusing and imaging, Phys. Rev. Appl. **15**, 024005 (2021).

[6] Z. Lin and S. Tol, Elastic metasurfaces for full wavefront control and low-frequency energy harvesting, J. Vib. Acoust. **143**, 061005 (2021).

[7] Y. Shen, Y. Xu, F. Liu, F. Wang, and Z. Yang, 3D-printed meta-slab for focusing flexural waves in broadband, Extreme Mech. Lett. **48**, 101410 (2021).

[8] S.-M. Yuan, A.-L. Chen, X.-Y. Du, H.-W. Zhang, B. Assouar, and Y.-S. Wang, Reconfigurable flexural waves manipulation by broadband elastic metasurface, Mech. Syst. Signal Process. **179**, 109371 (2022).

[9] Y. Jiang, Y. Liu, N. Hu, J. Song, and D. Lau, Continuous-phase-transformation elastic metasurface for flexural wave using notched structure, Int. J. Mech. Sci. **257**, 108563 (2023).

[10] Z.-L. Xu, D.-F. Wang, Y.-F. Shi, Z.-H. Qian, B. Assouar, and K.-C. Chuang, Arbitrary wavefront modulation utilizing an aperiodic elastic metasurface, Int. J. Mech. Sci. **255**, 108460 (2023).

[11] M. Jiang, Y.-F. Wang, B. Assouar, and Y.-S. Wang, Scattering-free modulation of elastic shear-horizontal waves based on interface-impedance theory, Phys. Rev. Appl. **20**, 054020 (2023).

[12] Y. Shen, Y. Xu, F. Liu, F. Wang, G. Wang, and Z. Yang, Broadband elastic energy harvesting based on achromatic meta-grating, Extreme Mech. Lett. **72**, 102253 (2024).

[13] B. Lin, J. Li, W. Lin, and Q. Ma, Active tunable elastic metasurface for abnormal flexural wave transmission, Appl. Sci. **14**, 2717 (2024).

[14] K. Su and L. Li, A Programmable metasurface based on acoustic black hole for real-time control of flexural waves, J. Appl. Phys. **135**, 133105 (2024).

[15] H. Zhu, X. Zhang, W. Liu, H. Long, Y. Cheng, and X. Liu, Unidirectional focusing for broadband Lamb guided wave based on mode conversion, Commun. Phys. **8**, 122 (2025).

[16] H. Zhu and F. Semperlotti, Anomalous refraction of acoustic guided waves in solids with geometrically tapered metasurfaces, Phys. Rev. Lett. **117**, 034302 (2016).
[17] Z. Lin, W. Xu, C. Xuan, W. Qi, and W. Wang, Modular elastic metasurfaces with mass oscillators for transmitted flexural wave manipulation, J. Phys. D: Appl. Phys. **54**, 255303 (2021).
[18] G. Ma, M. Yang, S. Xiao, Z. Yang, and P. Sheng, Acoustic metasurface with hybrid resonances, Nat. Mater. **13**, 873 (2014).
[19] J. Mei and Y. Wu, Controllable transmission and total reflection through an impedance-matched acoustic metasurface, New J. Phys. **16**, 123007 (2014).
[20] R. Zhu, X. Liu, G. Hu, C. Sun, and G. Huang, Negative refraction of elastic waves at the deep-subwavelength scale in a single-phase metamaterial, Nat. Commun. **5**, 5510 (2014).
[21] Y. Liu, Z. Liang, F. Liu, O. Diba, A. Lamb, and J. Li, Source illusion devices for flexural lamb waves using elastic metasurfaces, Phys. Rev. Lett. **119**, 034301 (2017).
[22] B. Assouar, B. Liang, Y. Wu, Y. Li, J. Cheng, and Y. Jing, Acoustic metasurfaces, Nat. Rev. Mater. **3**, 460 (2018).
[23] L. Cao, Z. Yang, Y. Xu, and B. Assouar, Deflecting flexural wave with high transmission by using pillared elastic metasurface, Smart Mater. Struct. **27**, 075051 (2018).
[24] Y. Xu, L. Cao, P. Peng, X. Zhou, B. Assouar, and Z. Yang, Beam splitting of flexural waves with a coding meta-slab, Appl. Phys. Express **12**, 097002 (2019).
[25] J. Zhang, X. Su, Y. Liu, Y. Zhao, Y. Jing, and N. Hu, Metasurface constituted by thin composite beams to steer flexural waves in thin plates, Int. J. Solids Struct. **162**, 14 (2019).
[26] J. Rong, W. Ye, S. Zhang, and Y. Liu, Frequency-coded passive multifunctional elastic metasurfaces, Adv. Funct. Mater. **30**, 2005285 (2020).
[27] H. Nassar, B. Yousefzadeh, R. Fleury, M. Ruzzene, A. Alù, C. Daraio, A. N. Norris, G. Huang, and M. R. Haberman, Nonreciprocity in acoustic and elastic materials, Nat. Rev. Mater. **5**, 667 (2020).
[28] K. Stojanoska and C. Shen, Non-Hermitian planar elastic metasurface for unidirectional focusing of flexural waves, Appl. Phys. Lett. **120**, 241701 (2022).
[29] T. Yang, Z. Lin, X. Zhu, and T. Yang, Elastic metasurface with dual-coupled resonators for highly efficient energy harvesting, Phys. Rev. Appl. **18**, 064065 (2022).
[30] W. Zhou, S. Wang, Q. Wu, X. Xu, X. Huang, G. Huang, Y. Liu, and Z. Fan, An inverse design paradigm of multifunctional elastic metasurface via data-driven machine learning, Mater. Des. **226**, 111560 (2023).
[31] P. Zhao, L. Luo, Y. Liu, and J. Li, Flexural wave illusion on a curved plate, APL Mater. **11**, 121103 (2023).
[32] F. Ma, Acoustic and mechanical metamaterials for various applications—A brief review, Front. Mater. **12**, 1626945 (2025).
[33] A. Díaz-Rubio and S. A. Tretyakov, Acoustic metasurfaces for scattering-free anomalous reflection and refraction, Phys. Rev. B **96**, 125409 (2017).
[34] J. Du, Z. Lin, S. T. Chui, W. Lu, H. Li, A. Wu, Z. Sheng, J. Zi, X. Wang, S. Zou, and F. Gan, Optical beam steering based on the symmetry of resonant modes of nanoparticles, Phys. Rev. Lett. **106**, 203903 (2011).
[35] N. Mohammadi Estakhri and A. Alù, Wave-front transformation with gradient metasurfaces, Phys. Rev. X **6**, 041008 (2016).
[36] A. Epstein and O. Rabinovich, Unveiling the properties of metagratings via a detailed analytical model for synthesis and analysis, Phys. Rev. Appl. **8**, 054037 (2017).
[37] D. Torrent, Acoustic anomalous reflectors based on diffraction grating engineering, Phys. Rev. B **98**, 060101(R) (2018).
[38] Y. Fu, Y. Cao, and Y. Xu, Multifunctional reflection in acoustic metagratings with simplified design, Appl. Phys. Lett. **114**, 053502 (2019).
[39] Y. K. Chiang, S. Oberst, A. Melnikov, L. Quan, S. Marburg, A. Alù, and D. A. Powell, Reconfigurable acoustic metagrating for high-efficiency anomalous reflection, Phys. Rev. Appl. **13**, 064067 (2020).
[40] L. Fan and J. Mei, Metagratings for waterborne sound: Various functionalities enabled by an efficient inverse-design approach, Phys. Rev. Appl. **14**, 044003 (2020).
[41] S. Y. Kim, W. Lee, J. S. Lee, and Y. Y. Kim, Longitudinal wave steering using beam-type elastic metagratings, Mech. Syst. Signal Process. **156**, 107688 (2021).

[42] S. Bernard, F. Chikh-Bled, H. Kourchi, F. Chati, and F. Léon, Broadband negative reflection of underwater acoustic waves from a simple metagrating: Modeling and experiment, Phys. Rev. Appl. **17**, 024059 (2022).
[43] Y. Hu, Y. Zhang, G. Su, M. Zhao, B. Li, Y. Liu, and Z. Li, Realization of ultrathin waveguides by elastic metagratings, Commun. Phys. **5**, 62 (2022).
[44] X. Li, D. Dong, J. Liu, Y. Liu, and Y. Fu, Perfect retroreflection assisted by evanescent guided modes in acoustic metagratings, Appl. Phys. Lett. **120**, 151701 (2022).
[45] Y. B. Oh, S. Y. Kim, S. H. Cho, J. S. Lee, and Y. Y. Kim, Near-perfect retroreflection of flexural waves via optimized elastic metagratings, Int. J. Mech. Sci. **262**, 108750 (2024).
[46] Y. Wang, Y. Cheng, and X. Liu, Modulation of acoustic waves by a broadband metagrating, Sci. Rep. **9**, 7271 (2019).
[47] Z. Hou, X. Fang, Y. Li, and B. Assouar, Highly efficient acoustic metagrating with strongly coupled surface grooves, Phys. Rev. Appl. **12**, 034021 (2019).
[48] J. Mei, L. Fan, and X. Hong, Elastic metagratings with simultaneous modulation of reflected and transmitted waves, Crystals **12**, 901 (2022).
[49] K. Sun, Y. Fan, S. Chen, F. Yang, J. Li, Q. Fu, and F. Zhang, Highly efficient transmissive wavefront steering with acoustic metagrating composed of Helmholtz-resonators, Mater. Des. **224**, 111352 (2022).
[50] X. Zhang, L. Li, K. Li, T. Liu, J. Zhang, and N. Hu, Flexural wave splitting via elastic metagratings based on high-order diffraction theory, Appl. Acoust. **202**, 109170 (2023).
[51] Y. Fu, C. Shen, Y. Cao, L. Gao, H. Chen, C. T. Chan, S. A. Cummer, and Y. Xu, Reversal of transmission and reflection based on acoustic metagratings with integer parity design, Nat. Commun. **10**, 2326 (2019).
[52] Y. Yang, H. Jia, Y. Bi, H. Zhao, and J. Yang, Experimental demonstration of an acoustic asymmetric diffraction grating based on passive parity-time-symmetric medium, Phys. Rev. Appl. **12**, 034040 (2019).
[53] B. Li, Y. Hu, J. Chen, G. Su, Y. Liu, M. Zhao, and Z. Li, Efficient asymmetric transmission of elastic waves in thin plates with lossless metasurfaces, Phys. Rev. Appl. **14**, 054029 (2020).
[54] L. Fan and J. Mei, Acoustic metagrating circulators: Nonreciprocal, robust, and tunable manipulation with unitary efficiency, Phys. Rev. Appl. **15**, 064002 (2021).
[55] H. Kourchi, S. Bernard, F. Chati, and F. Léon, Efficient asymmetrical transmission through a metagrating for underwater acoustic waves, Appl. Phys. Lett. **123**, 031702 (2023).
[56] L. Fan and J. Mei, Multifunctional waterborne acoustic metagratings: From extraordinary transmission to total and abnormal reflection, Phys. Rev. Appl. **16**, 044029 (2021).
[57] Z. Du and J. Mei, Metagrating-based acoustic wavelength division multiplexing enabled by deterministic and probabilistic deep learning models, Phys. Rev. Res. **4**, 033165 (2022).
[58] Y. Jin, X. Fang, Y. Li, and D. Torrent, Engineered diffraction gratings for acoustic cloaking, Phys. Rev. Appl. **11**, 011004(R) (2019).
[59] J. He, X. Jiang, D. Ta, and W. Wang, Experimental demonstration of underwater ultrasound cloaking based on metagrating, Appl. Phys. Lett. **117**, 091901 (2020).
[60] A. Song, C. Sun, Y. Xiang, and F. Xuan, Switchable acoustic metagrating for three-channel retroreflection and carpet cloaking, Appl. Phys. Express **15**, 024002 (2022).
[61] Z. Du and J. Mei, Wide-angle and high-efficiency acoustic retroreflectors enabled by many-objective optimization algorithm and deep learning models, Phys. Rev. Mater. **7**, 115201 (2023).
[62] Y. Jia and J. Mei, Omnidirectional retroreflectors based on flexural wave metagratings, J. Appl. Phys. **137**, 153105 (2025).
[63] Y. Fu, C. Shen, X. Zhu, J. Li, Y. Liu, S. A. Cummer, and Y. Xu, Sound vortex diffraction via topological charge in phase gradient metagratings, Sci. Adv. **6**, eaba9876 (2020).
[64] K. Zhao, H. Zou, Y. Xia, C. Wu, L. Xu, Y. Ge, S. Yuan, and H. Sun, Acoustic metagrating focusing and Bessel vortexes, Appl. Phys. Lett. **125**, 171702 (2024).
[65] Y.-J. Lu, H.-Y. Zou, J. Qian, Y. Wang, Y. Ge, S.-Q. Yuan, H.-X. Sun, and X.-J. Liu, Multifunctional reflected lenses based on aperiodic acoustic metagratings, Appl. Phys. Lett. **119**, 173501 (2021).
[66] J. Mei, L. Fan, and X. Hong, Broadband and high-numerical-aperture sharp focusing for waterborne sound with metagrating-based lens, New J. Phys. **24**, 093014 (2022).

[67] L. Fan and J. Mei, Flow-permeable and tunable metalens for subdiffraction waterborne-sound focusing, Phys. Rev. Appl. **19**, 024026 (2023).
[68] J. Mei, L. Fan, and X. Hong, Acoustic metalens with switchable and sharp focusing, Appl. Phys. Express **16**, 077002 (2023).
[69] L. Fan and J. Mei, Achromatic needle focusing with super-resolution enabled by a ring-shaped acoustic metalens, Phys. Rev. Appl. **20**, 054053 (2023).
[70] H. Peng, L. Fan, and J. Mei, Simultaneous manipulation of longitudinal and transverse elastic waves with a sharp focusing effect and customizable energy splitting ratios, J. Appl. Phys. **135**, 033102 (2024).
[71] Y. Jia and J. Mei, Ultrahigh-efficiency and superresolution focusing of the flexural wave enabled by a hybrid metalens with a large numerical aperture, Phys. Rev. Appl. **22**, 064094 (2024).
[72] L. Yin and J. Mei, Hybrid metalens for ultrawide-angle and high-efficiency focusing of waterborne sound, Phys. Rev. Appl. **24**, 064054 (2025).